

Fluctuation correction for the order–disorder transition of diblock copolymer melts

Cite as: J. Chem. Phys. 154, 124902 (2021); doi: 10.1063/5.0046167

Submitted: 1 February 2021 • Accepted: 5 March 2021 •

Published Online: 22 March 2021



View Online



Export Citation



CrossMark

T. M. Beardsley  and M. W. Matsen ^{a)} 

AFFILIATIONS

Department of Chemical Engineering, Department of Physics & Astronomy, and Waterloo Institute for Nanotechnology, University of Waterloo, Waterloo, Ontario N2L 3G1, Canada

^{a)} Author to whom correspondence should be addressed: mwmatsen@uwaterloo.ca

ABSTRACT

The order–disorder transition (ODT) of diblock copolymer melts is evaluated for an invariant polymerization index of $\bar{N} = 10^4$, using field-theoretic simulations (FTS) supplemented by a partial saddle-point approximation for incompressibility. For computational efficiency, the FTS are performed using the discrete Gaussian-chain model, and results are then mapped onto the continuous model using a linear approximation for the Flory–Huggins χ parameter. Particular attention is paid to the complex phase window. Results are found to be consistent with the well-established understanding that the gyroid phase extends down to the ODT. Furthermore, our simulations are the first to predict that the Fddd phase survives fluctuation effects, consistent with experiments.

Published under license by AIP Publishing. <https://doi.org/10.1063/5.0046167>

I. INTRODUCTION

The phase behavior of block copolymer melts is understood to be universal,¹ which implies that all systems can be represented by the standard Gaussian-chain model (GCM)² in the limit of high molecular weight. The GCM is a minimal model that treats a melt as an incompressible system of elastic threads interacting by pairwise contact forces. Its mean-field behavior for AB diblock copolymer, as predicted by self-consistent field theory (SCFT),^{2–6} is controlled by just three quantities: the composition f , the ratio of segment lengths a_A/a_B , and the product χN , where N is the number of segments of volume ρ_0^{-1} per molecule and χ is the effective Flory–Huggins interaction parameter.

In polymer field theory, the particle-based GCM is transformed into a mathematically equivalent field-based model, involving a composition field, $W_-(\mathbf{r})$, that couples to the difference between A and B concentrations, $\phi_-(\mathbf{r})$, and a pressure field, $W_+(\mathbf{r})$, that couples to the total concentration, $\phi_+(\mathbf{r})$, in a system of noninteracting polymers. The field-based Hamiltonian, $H[W_-, W_+]$, takes the form^{4–6}

$$\frac{H}{k_B T} = -n \ln Q + \rho_0 \int \left(\frac{\chi_b}{4} + \frac{W_-^2(\mathbf{r})}{\chi_b} - W_+(\mathbf{r}) \right) d\mathbf{r}, \quad (1)$$

where χ_b is the bare interaction parameter and $Q[W_-, W_+]$ is the partition function for a single molecule in an equivalent system of noninteracting polymers. Note that the constant in the integral, $\chi_b/4$, is typically dropped, but it will become relevant when we equilibrate the domain size.⁷

In SCFT, the free energy of the system is approximated by $F = H[w_-, w_+]$, where $w_-(\mathbf{r})$ and $w_+(\mathbf{r})$ denote the saddle point of the Hamiltonian. The saddle point is obtained by solving the self-consistent conditions $\mathcal{D}H/\mathcal{D}W_- = \mathcal{D}H/\mathcal{D}W_+ = 0$, where

$$\frac{1}{k_B T \rho_0} \frac{\mathcal{D}H}{\mathcal{D}W_-} = \phi_- + \frac{2}{\chi_b} W_-, \quad (2)$$

$$\frac{1}{k_B T \rho_0} \frac{\mathcal{D}H}{\mathcal{D}W_+} = \phi_+ - 1. \quad (3)$$

In general, there are multiple solutions corresponding to different metastable phases; the one of lowest free energy represents the stable phase. Figure 1(a) shows the resulting mean-field phase diagram in terms of the effective χ , which in SCFT is the same as the bare χ_b . In addition to the classical lamellar (L), cylindrical (C), and spherical (S and S_{cp}) phases, the diagram includes the gyroid (G) phase discovered in 1994^{8,9} and the Fddd (O^{70}) phase discovered in 2007.¹⁰

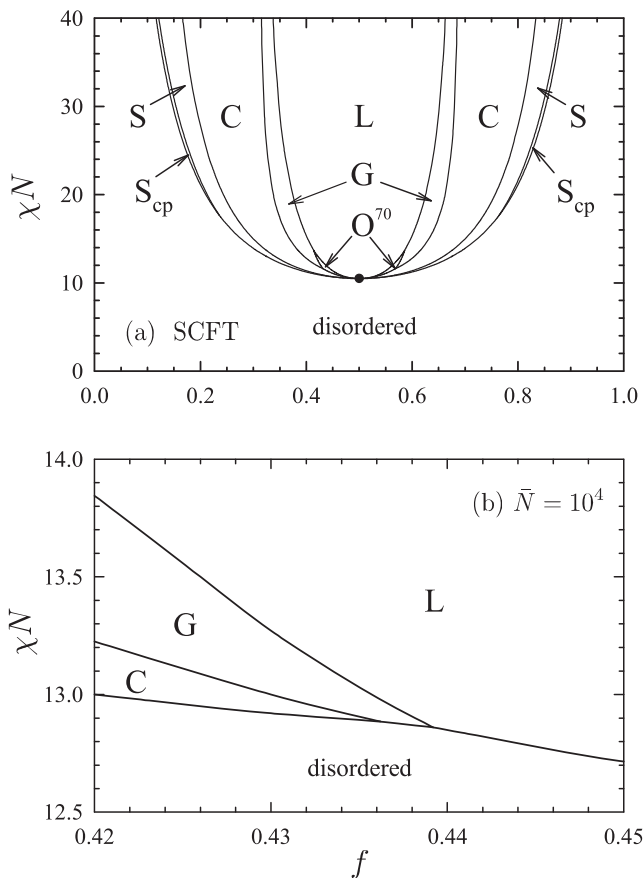


FIG. 1. (a) Mean-field phase diagram for conformationally symmetric diblock copolymer melts (i.e., $a_A = a_B$), calculated using SCFT. The ordered phases are lamellar (L), Fddd (O^{70}), gyroid (G), cylindrical (C), bcc spherical (S), and hcp spherical (S_{cp}). (b) Fluctuation-corrected phase diagram for $\tilde{N} = 10^4$, calculated by Miao and Wickham¹⁵ using Landau–Brazovskii theory.

However, contrary to experiments, only the spherical phases exhibit a direct transition with the disordered phase, apart from the critical lamellar–disorder transition at $f = 0.5$ [denoted by a dot in Fig. 1(a)].

Fluctuation corrections to the mean-field phase diagram were first addressed by Fredrickson and Helfand in 1987,¹¹ using a Landau–Brazovskii theory.¹² They showed that the corrections are controlled by the invariant polymerization index, $\tilde{N} = a^6 \rho_0^2 N$, where $a = [f a_A^2 + (1-f) a_B^2]^{1/2}$ is the average segment length. Typical values of \tilde{N} range from 10^2 to 10^4 .¹³ The initial calculation only considered the classical L, C, and S ordered phases, but Hamley and Podnec¹⁴ extended it to include the gyroid phase, and Miao and Wickham¹⁵ later accounted for the Fddd phase. The resulting phase diagram is displayed in Fig. 1(b) for $\tilde{N} = 10^4$. Consistent with experiments, the critical point is destroyed creating direct transitions between the different ordered phases and the disordered phase. Although it predicts a gyroid–disorder transition, which is consistent with experiments, the fluctuations cause Fddd to become unstable, which is inconsistent with its observation in PS-PI diblocks of $\tilde{N} \approx 1.1 \times 10^3$. This omission is not surprising given that the theory also fails to predict a

stable S phase.¹¹ Indeed, Fredrickson and Helfand pointed out that the approximations involved are only accurate for $\tilde{N} \gtrsim 10^{10}$.

Field-theoretic simulations (FTS) provide a means of obtaining accurate fluctuation corrections, by simulating the Hamiltonian, $H[W_-, W_+]$.^{6,16,17} However, standard simulation techniques are not applicable. Although the composition field, $W_-(\mathbf{r})$, takes on real values, the pressure field, $W_+(\mathbf{r})$, is imaginary, which leads to a complex-valued Hamiltonian and, thus, a Boltzmann weight that is not positive definite. Fredrickson *et al.* dealt with this by performing complex Langevin simulations (CL-FTS).^{16,17}

In 2008, Lennon *et al.*¹⁸ evaluated fluctuation corrections to the ODT of diblock copolymer melts using CL-FTS. The simulations predicted direct transitions between the disordered phase and the ordered lamellar, gyroid, and cylindrical phases. They never considered sufficient asymmetries to observe the spherical phase, nor did they consider the Fddd phase although it had been predicted by SCFT several years prior.¹⁹ The simulations, however, were limited to an invariant polymerization index of $\tilde{N} = 5.4 \times 10^5$, which far exceeds that of experiments. They were unable to consider smaller \tilde{N} because of an instability in the complex Langevin dynamics.^{20,21}

Delaney and Fredrickson²² have since tamed the instability by introducing compressibility and smearing the concentrations (or, equivalently, smearing the interactions), which allowed them to generate a phase diagram for $\tilde{N} \approx 10^4$. However, their fluctuation corrections destroy the Fddd phase while still remaining insufficient to produce a direct gyroid–disorder transition. They suggested that the experimental observation of Fddd may be a result of conformational asymmetry (i.e., $a_A \neq a_B$), but this is hard to reconcile with the fact that Fddd has been identified on both sides of the phase diagram.²³ If the asymmetry disfavors Fddd on one side, then it should favor Fddd on the other side.²⁴ Another suggestion was that the simple pairwise interactions used in the simulations may be insufficient to model PI-PS diblocks. Hopefully, this is not the case, as it would imply a breakdown in universality despite the reasonably high $\tilde{N} \approx 1.1 \times 10^3$.

An alternative strategy in FTS is to perform a partial saddle-point approximation,^{25,26} where $W_-(\mathbf{r})$ fluctuates while the pressure field follows its saddle point, $w_+(\mathbf{r})$, which turns out to be real. Consequently, the resulting Hamiltonian, $H[W_-, w_+]$, is also real, which then allows for standard simulation techniques. Ordinary Langevin simulations (L-FTS) have so far proven to be the most efficient choice.²⁷ Comparisons with CL-FTS have shown the partial saddle-point approximation to be relatively accurate.^{26,28} An important advantage of the approximation is that it removes the instability, facilitating simulations at lower \tilde{N} .^{27,29,30}

In FTS, the fields are represented on a discrete grid with some finite spacing, Δ . One might expect results to become increasingly accurate as $\Delta \rightarrow 0$, but this is not the case for the standard GCM due to an ultraviolet (UV) divergence. Olvera de la Cruz *et al.*³¹ were the first to investigate the divergence and showed that it could be removed by expressing results in terms of the renormalization interaction parameter,

$$\chi = \left(1 - \frac{6\alpha}{\pi^2} l \Lambda\right) \chi_b, \quad (4)$$

where $\alpha = 1.221375$ for cubic grids,^{27,32} $l \equiv 1/\rho_0 a^2$ is the packing length, and $\Lambda \equiv \pi/\Delta$ is a wavevector cutoff. Grzywacz *et al.*³³ have since provided more rigorous evidence that the theory is, indeed,

renormalizable. Stasiak and Matsen³² demonstrated that the renormalization works well for large \bar{N} , but Vorselaars and Matsen²⁹ found that it starts to fail just as the experimentally relevant regime is approached. Beardsley and Matsen³⁰ addressed this problem by applying the Morse calibration,

$$\chi = z_\infty \chi_b + c_2 \chi_b^2 + c_3 \chi_b^3 + \dots, \quad (5)$$

devised for particle-based simulations.^{34–36} The first coefficient, z_∞ , is the relative number of intermolecular contacts in the limit of $\chi_b \rightarrow 0$ and $N \rightarrow \infty$, while the remaining coefficients are determined by fitting the peak of the disordered-state structure function, $S(k^*)$, to renormalized one-loop (ROL) predictions.^{33,37} They also showed that the renormalization in Eq. (4) equates to the linear approximation $\chi \approx z_\infty \chi_b$. Delaney and Fredrickson²² avoided the UV divergence altogether when they modified the model by including compressibility and smearing the interactions. However, doing so requires mapping the parameters of the modified model back onto those of the standard GCM, which could, likewise, be accomplished with the Morse calibration.

Here, we again examine the ODT of diblock copolymer melts for $\bar{N} = 10^4$, but this time using FTS supplemented by the partial saddle-point approximation. To avoid numerical errors associated with integrations along the contours of continuous chains, we switch to a bead–spring model. We, nevertheless, retain the zero-range contact forces and the incompressibility condition. To remove the UV divergence and to account for the change in the model, we express results in terms of the linear $\chi \approx z_\infty \chi_b$, which should be reasonably accurate given the large value of \bar{N} .³⁰

II. FIELD-THEORETIC SIMULATIONS

Our FTS follow the implementation in Refs. 6 and 27, except that we now switch from continuous to discrete chains so as to avoid numerical errors associated with integrations along the contours of continuous chains. The first N_A monomers are A-type, while the remaining $N_B = N - N_A$ monomers are B-type, which leads to a composition of $f = N_A/N$. The bonds are harmonic all with equal statistical lengths of a such that the molecules are conformationally symmetric with an unperturbed end-to-end length of $R_0 = a\sqrt{\bar{N}}$. Although the monomers are treated as point particles, they are each assigned a finite volume of ρ_0^{-1} . As a result, the total number of molecules is

$$n = \frac{V\rho_0}{N} = \frac{V}{R_0^3} \sqrt{\bar{N}}, \quad (6)$$

where V is the volume of the system.

The current study is performed for a polymerization of $N = 90$ and a monomer density, ρ_0 , adjusted such that $\bar{N} \equiv a^6 \rho_0^2 N = 10^4$. The simulations are generally conducted in orthorhombic boxes of size $V = L_x L_y L_z$, using periodic boundary conditions. All spatially dependent quantities are specified at the vertices of an $m_x \times m_y \times m_z$ grid with a regular spacing of $\Delta_\alpha = L_\alpha/m_\alpha$ in each direction α . Hence, each grid point corresponds to a volume of $V_{\text{cell}} = \Delta_x \Delta_y \Delta_z$.

The switch to discrete chains does not alter the Hamiltonian in Eq. (1), but it does change the statistical mechanics for the system of noninteracting polymers.³⁸ Nevertheless, the calculation proceeds in much the same way. A partial partition function, $q_i(\mathbf{r})$, is defined

for the first i monomers of a discrete chain with its i th monomer constrained to position \mathbf{r} . However, instead of satisfying a diffusion equation, it satisfies the recursion relation

$$q_{i+1}(\mathbf{r}) = h_{i+1}(\mathbf{r}) \int g(R) q_i(\mathbf{r} - \mathbf{R}) d\mathbf{R}, \quad (7)$$

subject to the initial condition $q_1(\mathbf{r}) = h_1(\mathbf{r})$.³⁸ Here,

$$g(R) = \left(\frac{3}{2\pi a^2} \right)^{3/2} \exp\left(-\frac{3R^2}{2a^2} \right) \quad (8)$$

is a Boltzmann weight for the bond potential and

$$h_i(\mathbf{r}) = \exp(-W_+(\mathbf{r}) - \gamma_i W_-(\mathbf{r})) \quad (9)$$

is a Boltzmann weight for the field energy acting on the i th monomer. To distinguish the two components, we define $\gamma_i = 1$ for A monomers (i.e., $i \leq N_A$) and $\gamma_i = -1$ for B monomers (i.e., $i > N_A$). The calculation also requires an analogous partial partition function, $q_i^\dagger(\mathbf{r})$, for the last $N + 1 - i$ monomers of the chain, which is obtained by iterating

$$q_{i-1}^\dagger(\mathbf{r}) = h_{i-1}(\mathbf{r}) \int g(R) q_i^\dagger(\mathbf{r} - \mathbf{R}) d\mathbf{R}, \quad (10)$$

starting from $q_N^\dagger(\mathbf{r}) = h_N(\mathbf{r})$.

The recursion relation in Eq. (7) is calculated by switching back and forth between real and reciprocal space using fast Fourier transforms. The convolution integral is first evaluated in reciprocal space, where it reduces to a simple multiplication of $g(k) = \exp(-a^2 k^2/6)$ and $q_i(\mathbf{k})$. The integral is then converted back to real space and multiplied by $h_{i+1}(\mathbf{r})$ to give $q_{i+1}(\mathbf{r})$. The second recursion relation in Eq. (10) is solved in an analogous manner.

Once both partial partition functions have been obtained, the single-chain partition function is given by

$$Q = \frac{1}{V} \int \frac{q_i(\mathbf{r}) q_i^\dagger(\mathbf{r})}{h_i(\mathbf{r})} d\mathbf{r}. \quad (11)$$

The integral can be evaluated using any value of $1 \leq i \leq N$, but one typically chooses $i = N$. We also require the composition and total concentration in the system of noninteracting polymers, which are given by

$$\phi_-(\mathbf{r}) = \frac{1}{NQ} \sum_{i=1}^N \gamma_i \frac{q_i(\mathbf{r}) q_i^\dagger(\mathbf{r})}{h_i(\mathbf{r})}, \quad (12)$$

$$\phi_+(\mathbf{r}) = \frac{1}{NQ} \sum_{i=1}^N \frac{q_i(\mathbf{r}) q_i^\dagger(\mathbf{r})}{h_i(\mathbf{r})}, \quad (13)$$

respectively.

A. Langevin dynamics

As mentioned in the Introduction, we reduce the FTS to a single fluctuating field, $W_-(\mathbf{r})$, by applying the partial saddle-point approximation, whereby $W_+(\mathbf{r})$ is replaced by $w_+(\mathbf{r})$. The saddle point, $w_+(\mathbf{r})$, is updated every time $W_-(\mathbf{r})$ changes using Anderson mixing,^{39,40} following an analogous implementation⁴¹ to that of Ref. 42. The iterations continue until the incompressibility condition, $\phi_+(\mathbf{r}) = 1$, is satisfied to an error tolerance of $\varepsilon = 10^{-4}$.

A Markov sequence of equilibrated configurations is generated by evolving the remaining field, $W_-(\mathbf{r}; \tau)$, using Langevin dynamics,

$$W_-(\mathbf{r}; \tau + \delta\tau) = W_-(\mathbf{r}; \tau) - \Lambda_i \delta\tau + \mathcal{N}(0, \sigma), \quad (14)$$

where τ is the simulation time and $\mathcal{N}(0, \sigma)$ provides a random number generated from a normal distribution of zero mean and $\sigma^2 = 2\delta\tau/V_{\text{cell}}\rho_0$ variance. To improve accuracy, we apply the predictor–corrector algorithm.^{27,43} A predicted field at $\tau + \delta\tau$ is first obtained using Eq. (14) with

$$\Lambda_1 = \phi_-(\mathbf{r}; \tau) + \frac{2}{\chi_b} W_-(\mathbf{r}; \tau), \quad (15)$$

and then, a corrected field is obtained with

$$\Lambda_2 = \frac{1}{2} \left[\Lambda_1 + \phi_-(\mathbf{r}; \tau + \delta\tau) + \frac{2}{\chi_b} W_-(\mathbf{r}; \tau + \delta\tau) \right], \quad (16)$$

evaluated using the predicted field. Note that the predictor and corrector steps use the same random number.

The optimum step size, $\delta\tau$, is determined by maximizing the ratio of simulation time to computational time, the latter of which is proportional to the cumulative number of Anderson mixing iterations, n_{mix} .²⁷ As illustrated in Fig. 2(a), the optimum value varies from $\delta\tau N = 0.6$ to 1.0 over the range of compositions considered in our study. It is also important to ensure that the finite size of $\delta\tau$ does not significantly impact the accuracy of the algorithm. As a rule of thumb, the difference between $\Lambda_1 \delta\tau$ and $\Lambda_2 \delta\tau$ should be small relative to the typical change in $W_-(\mathbf{r}; \tau)$, the magnitude of which is given by σ . Figure 2(b) confirms that this requirement is well satisfied.

As usual, the Langevin dynamics are applied for a sufficient amount of time (e.g., $\Delta\tau N \sim 10^5$ – 10^6) to equilibrate the system, before observables are sampled typically once every ten $\delta\tau$ steps. To detect the ODT, we collect statistics for the structure function,

$$\frac{S(k)}{\rho_0 N} = \frac{n}{(\chi_b V)^2} \langle |W_-(\mathbf{k})|^2 \rangle - \frac{1}{2\chi_b N}, \quad (17)$$

over a duration of $\Delta\tau N \sim 10^4$.

B. Effective interaction parameter

Justified by our large $\tilde{N} = 10^4$, we use the linear approximation, $\chi \approx z_\infty \chi_b$, for the effective interaction parameter. Here, z_∞ represents the relative number of intermolecular contacts of infinitely long polymers in an athermal melt. These limits correspond to zero fields, and thus, z_∞ can be calculated analytically, as outlined in Ref. 30. The calculation requires the probability, P_i , that two monomers of a chain, separated by i bonds along the contour, occupy the same cell of the grid. Generalizing the previous result to our orthorhombic grid, we obtain

$$P_i = \prod_\alpha \frac{1}{m_\alpha} \sum_{k_\alpha} e^{-a^2 k_\alpha^2 i/6}, \quad (18)$$

which in the thermodynamic limit (i.e., $m_\alpha \rightarrow \infty$) reduces to

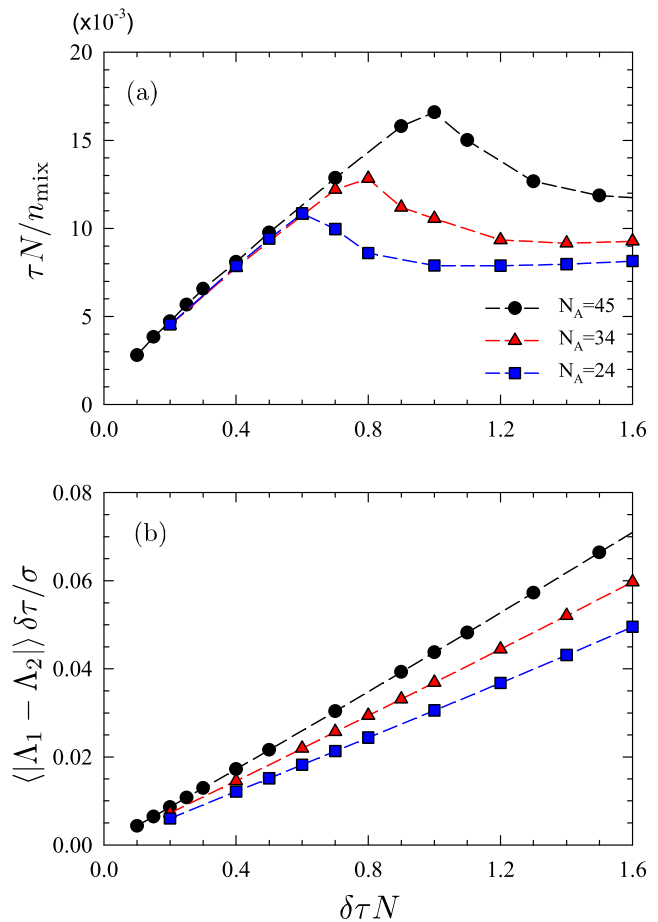


FIG. 2. (a) Simulation time, τ , in relation to the computation cost, n_{mix} , and (b) relative difference in the predicted and corrected fields plotted as a function of step size, $\delta\tau$. Results are obtained at different compositions, N_A , on the disordered side of the ODT. The peak in τ/n_{mix} identifies the optimum step size, and the small difference between Λ_1 and Λ_2 ensures the accuracy of the predictor–corrector algorithm.

$$P_i = \prod_\alpha \frac{\Delta_\alpha}{a} \sqrt{\frac{3}{2\pi i}} \operatorname{erf}\left(\frac{\pi a}{\Delta_\alpha} \sqrt{\frac{i}{6}}\right). \quad (19)$$

With this, we obtain

$$z_\infty = 1 - \frac{1}{V_{\text{cell}}\rho_0} \left[1 + 2 \sum_{i=1}^{\infty} P_i \right], \quad (20)$$

where the quantity in square brackets is the number of intramolecular contacts and $V_{\text{cell}}\rho_0$ is the total number of contacts experienced by a given monomer. Note that the intramolecular contacts include the term $P_0 = 1$ to account for self-interactions in the Gaussian-chain model.

The effectiveness of the calibration is well illustrated by comparing the structure function, $S(k)$, at different grid resolutions. Figure 3(a) demonstrates what happens if the divergence is ignored. If $\chi_b N$ is simply held constant, the segregation will decrease as $\Delta = L/m \rightarrow 0$, which is evident by a reduction in the peak height.

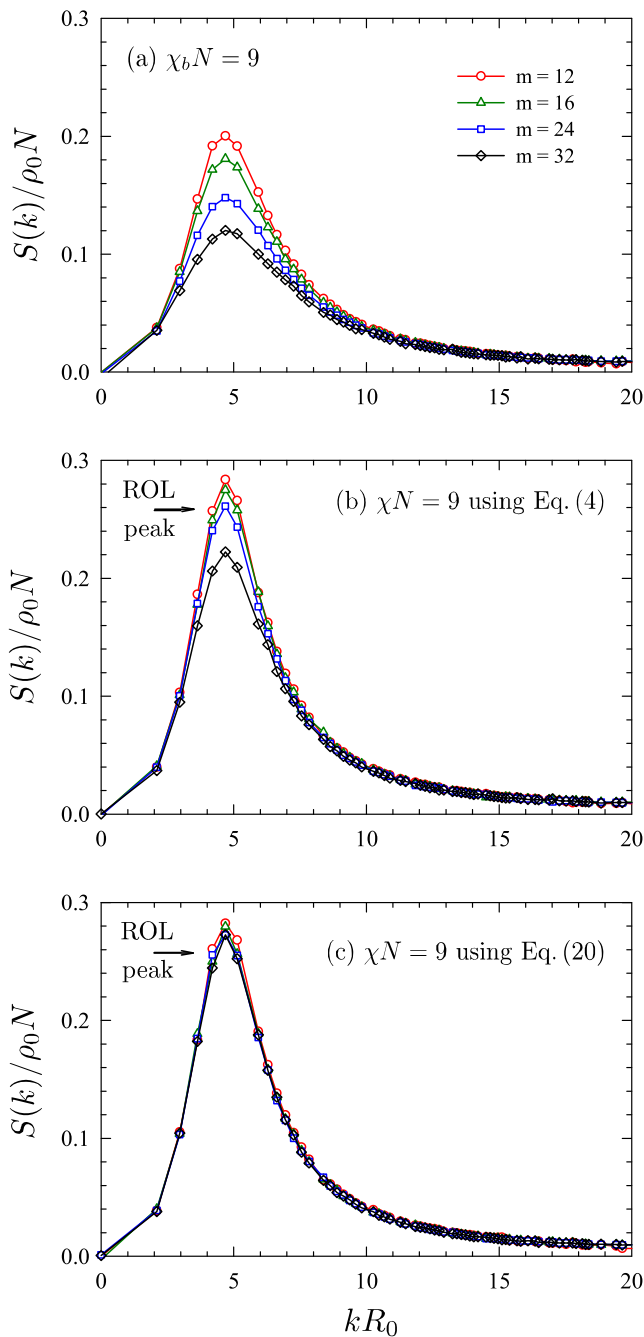


FIG. 3. Structure function, $S(k)$, for symmetric diblocks obtained in a cubic simulation box of size $L/aN^{1/2} = 3$ with different numbers of grid points, $m = L/\Delta$. (a) shows results for $\chi_b N = 9$ without any calibration, while (b) and (c) show results for $\chi N = 9$ defined by Eqs. (4) and (20), respectively. Arrows mark the peak height predicted by ROL.

This is partially corrected for in Fig. 3(b), where the comparison is performed at $\chi N = z_\infty \chi_b N = 9$, using the z_∞ from Eq. (4) derived for continuous Gaussian chains. This renormalization works well at low resolutions, where discrete chains are well approximated by

continuous chains, but it fails for small Δ . Figure 3(c) repeats the comparison, this time using the z_∞ from Eq. (20) derived for discrete chains. This results in good agreement over the full range of resolutions. It is worth noting that the resulting peak height of $S(k)$ agrees reasonably well with the ROL prediction, which adds to our justification for the linear χ . We have also performed similar tests for the ordered lamellar phase over the typical range of resolutions used in our simulations, and the predictions of $S(k)$ for different grids remain virtually indistinguishable.

C. Box-altering move

Equilibration of the domain size remains an outstanding problem for triply periodic phases, due to the fact that the UV divergence has a dependence on the density of grid points. However, Vorselaars *et al.*²⁹ demonstrated an effective method for the lower-dimensional lamellar or cylindrical phase, which conserves the volume of the simulation box. To apply it, lamellae are oriented normal to the x direction or cylinders are aligned with the x direction. The periodicity is then equilibrated by allowing the aspect ratio $\lambda(\tau)$ of the box dimensions $L_x = \lambda L_{x,0}$, $L_y = \lambda^{-1/2} L_{y,0}$, and $L_z = \lambda^{-1/2} L_{z,0}$ to vary from its initial value, $\lambda(0) = 1$.

In the spirit of the Langevin simulations, we evolve $\lambda(\tau)$ according to

$$\lambda(\tau + \delta\tau) = \lambda(\tau) - \frac{0.01}{nk_B T} \frac{dH}{d\lambda}, \quad (21)$$

where 0.01 is large enough that $\lambda(\tau)$ reaches equilibrium quickly but small enough that simple Euler steps are accurate. In principle, Eq. (21) should include a noise term, but it is irrelevant because $\lambda(\tau)$ is just one degree of freedom among many. Figure 4 shows a sample run in a simulation box containing three lamellae, where the initial box size is obtained from SCFT (i.e., $L_{x,0} = L_{y,0} = L_{z,0} = 3D_{\text{SCFT}}$). Once equilibrium is achieved, the preferred lamellar periodicity is determined from the average value of L_x denoted by the dashed line (i.e., $D = \langle L_x \rangle / 3$). Subsequent simulations are then run in simulation boxes of fixed dimensions commensurate with the preferred domain size.

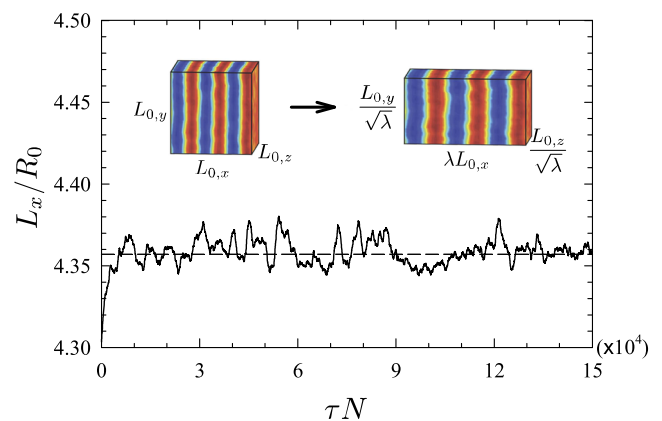


FIG. 4. Box move showing the relaxation of the lamellar period at $\chi N = 12.8$ and $f = 0.5$, starting from the SCFT prediction, $D/R_0 = 1.435$. The dashed line denotes the equilibrated box size, obtained by averaging over large τ .

The derivative of the Hamiltonian with respect to λ in Eq. (21) is calculated analytically using

$$\frac{1}{nk_B T} \frac{dH}{d\lambda} = -\frac{1}{\lambda Q} \left(L_x \frac{\partial Q}{\partial L_x} - \frac{L_y}{2} \frac{\partial Q}{\partial L_y} - \frac{L_z}{2} \frac{\partial Q}{\partial L_z} \right) + \frac{1}{V} \int \left(\frac{1}{4} - \frac{W_-^2(\mathbf{r})}{\chi_b^2} \right) d\mathbf{r} \times \frac{\partial \chi_b N}{\partial \lambda}. \quad (22)$$

The partial derivatives of Q with respect to the dimensions of the simulation box, L_α , are given by⁴⁴

$$\frac{\partial Q}{\partial L_\alpha} = -\frac{a^2}{3VL_\alpha} \sum_{i=1}^{N-1} \int q_i(\mathbf{r}) \frac{\partial^2}{\partial \alpha^2} \frac{q_i^\dagger(\mathbf{r})}{h(\mathbf{r})} d\mathbf{r}, \quad (23)$$

which we evaluate in reciprocal space using

$$\frac{\partial Q}{\partial L_\alpha} = \frac{a^2}{3(2\pi)^3 VL_\alpha} \sum_{i=1}^{N-1} \int q_i(\mathbf{k}) k_\alpha^2 g(k) q_{i+1}^\dagger(-\mathbf{k}) d\mathbf{k}. \quad (24)$$

The remaining partial derivative is evaluated holding $\chi = z_\infty \chi_b$ constant, for which

$$\frac{\partial \chi_b N}{\partial \lambda} = -\frac{\chi_b N}{z_\infty} \frac{dz_\infty}{d\lambda}. \quad (25)$$

Note that the 1/4 in the integral of Eq. (22) was overlooked in earlier studies of the lamellar phase.^{29,45} Nevertheless, its effect proves to be relatively minor, and so, they would have still obtained sufficiently accurate lamellar periods.

III. RESULTS

In our previous study²⁷ of symmetric diblocks at $\tilde{N} = 10^3$, we located the ODT using continuous thermodynamic integration.⁴⁵ Figure 5 demonstrates a similar attempt at $\tilde{N} = 10^4$, using the same step size of $\Delta\chi_b N = 10^{-6}$. The integration for the free energy of the lamellar phase, F_L , starts from a lamellar morphology at $\chi N = 13.05$, which abruptly disorders at $\chi N \approx 12.66$, while the one for the disordered phase, F_{dis} , starts from a disordered morphology at $\chi N = 12.43$, which spontaneously orders at $\chi N \approx 12.89$. The relative free energies of the two phases are determined by thermodynamic integration from an Einstein crystal (not shown), which serves as a reference system of known free energy.¹⁸ Based on the calibration, the ODT (i.e., $F_L = F_{\text{dis}}$) occurs at $\chi N \approx 12.68$. However, additional independent runs reveal that there is a significant error in this estimate. The problem is that the free energy difference is nearly an order of magnitude smaller than it was for $\tilde{N} = 10^3$. Nevertheless, the abrupt transitions between order and disorder bracket the equilibrium ODT within the interval 12.78 ± 0.12 . Furthermore, reducing the integration step to $\Delta\chi_b N = 2.5 \times 10^{-5}$ narrows the interval to 12.71 ± 0.01 , which provides a reliable and accurate estimate of the ODT.

Unfortunately though, the thermodynamic integration for non-lamellar phases proves to be problematic. The free energy curves become noisy with no well-defined kinks to indicate a switch in morphology. We attribute this to the relative ease of forming defects. Once a critical nucleus of the lamellar phase forms, the rest of the

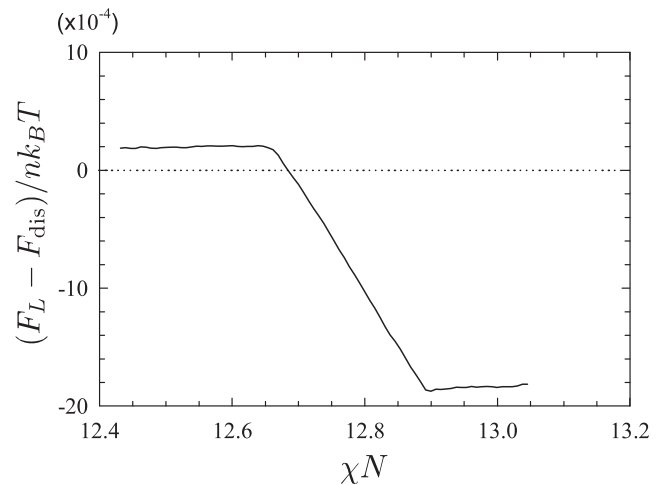


FIG. 5. Free energy difference between the lamellar and disordered phases of $N_A = N_B = 45$ diblocks, obtained from thermodynamic integration. The kinks at small and large χN result when the metastable phase switches to the stable phase.

melt is quickly pulled into alignment forming a defect-free morphology, as evident by sharp kinks in the free energy curve. In contrast, a network phase, such as gyroid, forms with multiple low-energy defects that correct themselves in a prolonged series of small but sudden rearrangements, resulting in the noisy behavior.

While small free energies and a lack of metastability cause problems for thermodynamic integration, they are an advantage for another approach. The ease of forming defects limits the degree to which ordered phases can survive superheating (i.e., exist at χN values below the ODT). Experiments typically determine the ODT by monitoring the disappearance of scattering peaks as the temperature is slowly increased. Similarly, we conclude that the best way to locate the ODT is to monitor the peaks of the structure function, $S(k)$, as χN is slowly decreased. As we narrow in on the ODT, we can focus our computational resources on the most weakly segregated configurations to ensure that the peaks are in equilibrium.

A. Lamellar-disorder transition

We begin by demonstrating our approach on the lamellar-disorder transition. The first step involves estimating the position of the ODT by performing scans up and down in χN , using cubic simulation boxes of $L_\alpha = 3D_{\text{SCFT}}$. Once the approximate ODT is determined, the lamellar period, D , is refined using the box move. The equilibrium period is generally about 1% larger than the SCFT prediction. Next, starting slightly above the ODT, we evaluate the structure function, $S(k)$, at a series of χN values separated by units of 0.1.

Figure 6 displays a sample of the $S(k)$ curves for $N_A = 40$. The solid triangles mark the expected peak positions for the lamellar phase. Strong lamellar peaks are observed at $\chi N = 13.7$, which gradually weaken as χN is reduced and ultimately disappear at $\chi N = 13.1$. To ensure that the lamellar phase is, indeed, stable at $\chi N = 13.2$, we run the simulations for an extra $\Delta\tau N \approx 5 \times 10^5$. The peaks

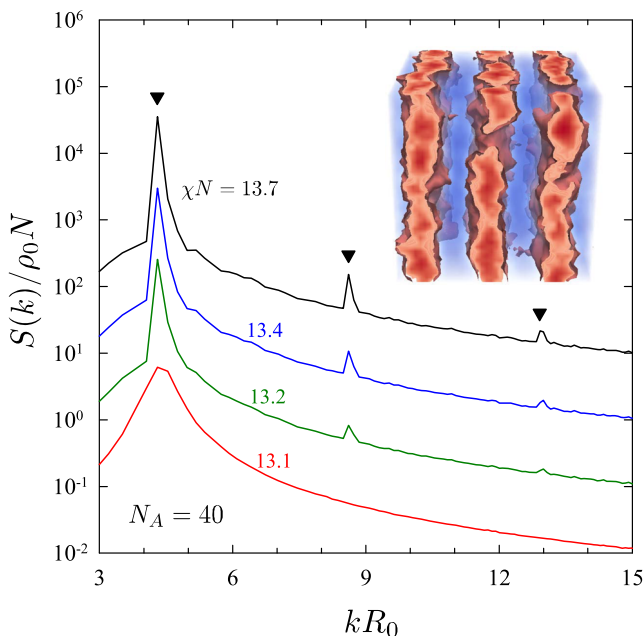


FIG. 6. Structure function, $S(k)$, at a sequence of χN values, calculated for diblocks with $N_A = 40$ and $N_B = 50$. For clarity, the curves for the ordered states exhibiting peaks are shifted up by an integer number of decades. The morphology (see the inset) and peak positions (triangles) confirm that the ordered state is lamellar.

remain, and thus, we conclude that the ODT occurs at $(\chi N)_{\text{ODT}} = 13.15 \pm 0.05$.

Table I lists the results for a range of compositions. For $N_A = 45$, the transition occurs at $(\chi N)_{\text{ODT}} = 12.75 \pm 0.05$, which is consistent with the metastability interval of 12.71 ± 0.01 produced by our slower thermodynamic integration. Thus, the calculations of $S(k)$ appear to be free of significant non-equilibrium effects. This should be even more so for the non-lamellar phases, where there is even less of a barrier to disordering.

B. Fddd-disorder transition

By $N_A = 38$, disordered melts no longer order into a lamellar morphology. Instead, they order into a network structure reminiscent of the Fddd phase, but of course, it cannot possibly have the correct symmetry on account of the cubic simulation box. SCFT predicts an orthorhombic unit cell of relative dimensions 1.00:2.02:3.57.

TABLE I. Lamellar-disorder transitions, sizes of the simulation box, and the z_∞ for our $40 \times 40 \times 40$ grid.

N_A	$(\chi N)_{\text{ODT}}$	L_α/R_0	z_∞
45	12.75	4.36	0.765
44	12.75	4.36	0.765
42	12.95	4.37	0.766
40	13.15	4.38	0.767
39	13.35	4.39	0.768

Given that $D_y \approx 2D_x$, we switched to a simulation box with appropriate values of $L_x = L_y$ and L_z for two unit cells of Fddd. Given the appropriate box, the disordered phase now spontaneously orders into the Fddd phase. The morphology is slightly distorted compared to the SCFT prediction, but the distortion vanishes when the dimensions of the simulation box are increased by a couple of percent.

The Fddd structure is then periodically repeated in the x and y directions to produce 8 unit cells in a simulation box that is relatively cubic. In the absence of the box move, we optimize the box size (with the fixed aspect ratios predicted by SCFT) by examining the Bragg peaks of $S(k)$. The peaks are found to be the strongest when the box is about 1.5% larger than the SCFT prediction, implying that the box is commensurate with the preferred dimensions of the morphology. Next, as we did for the lamellar phase, the structure function is calculated for a series of χN values.

The curves for $S(k)$, some of which are plotted in Fig. 7, exhibit a large number of peaks as a result of the orthorhombic unit cell, but nevertheless, all the peaks coincide with the allowed crystallographic reflections of the Fddd space-group symmetry,⁴⁶ which are marked by triangles. As before, the peaks weaken as χN is reduced, eventually disappearing at $\chi N = 13.4$. The run at $\chi N = 13.5$ is equilibrated for a prolonged time to ensure that Fddd remains stable, implying an ODT of $(\chi N)_{\text{ODT}} = 13.45 \pm 0.05$. To further ensure that the box size is optimum, we confirm that increasing or decreasing the box size by 1% reduces the stability of Fddd. Table II lists the estimated ODT for several other compositions. Note that we were unable to locate an Fddd-disorder transition at $N_A = 39$; the Fddd phase converts to a lamellar morphology prior to disordering.

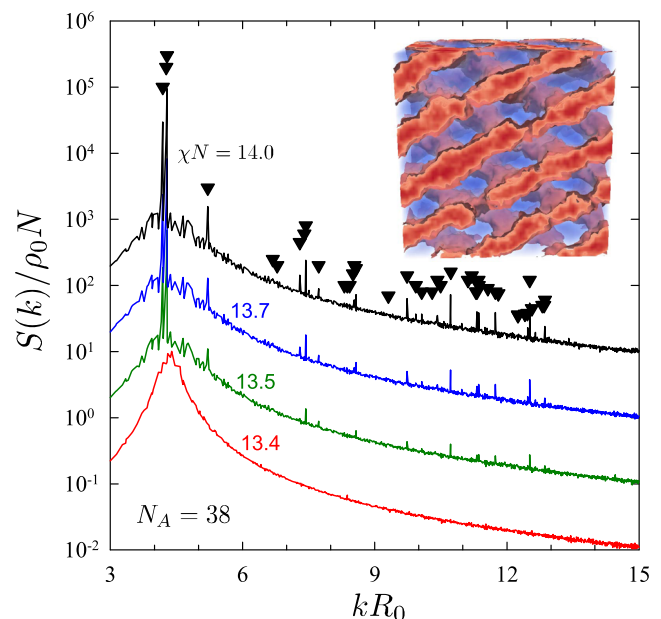


FIG. 7. Analogous plot to that of Fig. 6, but for diblocks with $N_A = 38$ and $N_B = 52$. The morphology (see the inset) and peak positions (triangles) confirm that the ordered state is Fddd.

TABLE II. Fddd-disorder transitions, sizes of the simulation box ($L_x = L_y$), and the z_∞ for our $64 \times 64 \times 56$ grid.

N_A	$(\chi N)_{\text{ODT}}$	L_y/R_0	L_z/R_0	z_∞
38	13.45	6.76	6.00	0.757
37	13.55	6.70	5.94	0.754
36	13.85	6.71	5.95	0.754

C. Gyroid-disorder transition

At $N_A = 36$, a single unit cell of the gyroid phase spontaneously forms from disorder for cubic boxes in the range $3.55R_0 \lesssim L_\alpha \lesssim 3.83R_0$. For smaller boxes, a cylinder phase forms, and for larger boxes, we observe perforated lamellae. To better estimate the preferred size, we periodically double the simulation boxes in each dimension creating 8 unit cells of gyroid, and then, we equilibrate and evaluate $S(k)$ at $\chi N = 13.9$. Based on the peak amplitudes, we estimate the preferred size of the unit cell to be $D = 3.66R_0$, which is about 3% larger than the SCFT prediction.

As before, we monitor the peaks of $S(k)$ as χN is reduced. A sample of the results is plotted in Fig. 8, from which we estimate an ODT of $(\chi N)_{\text{ODT}} = 13.75 \pm 0.05$. Estimates for other compositions are listed in Table III. Based on these, gyroid is less stable than Fddd for $N_A \geq 37$, but more stable for $N_A \geq 36$. For $N_A = 37$, where the relative stability is closest, we test whether decreasing or increasing the box size of either phase by 1% enhances its stability. It, in fact, does not, illustrating again that our box sizes are close to optimum.

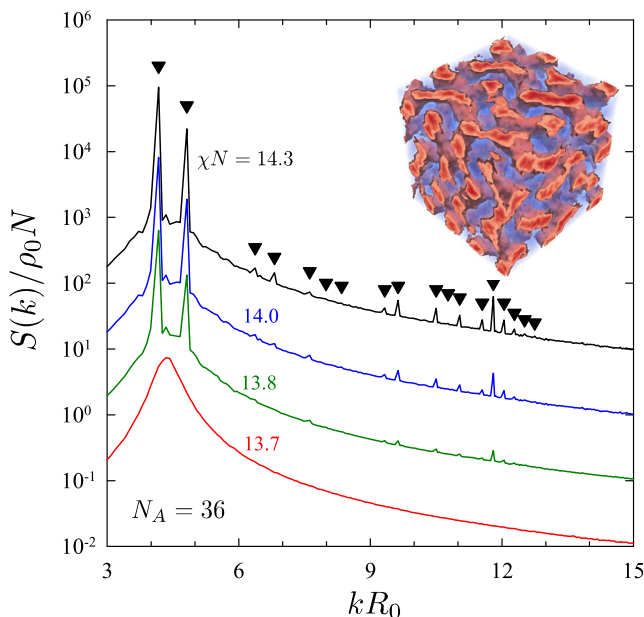


FIG. 8. Analogous plot to that of Fig. 6, but for diblocks with $N_A = 36$ and $N_B = 54$. The morphology (see the inset) and peak positions (triangles) confirm that the ordered state is gyroid.

TABLE III. Gyroid-disorder transitions, sizes of the simulation box, and the z_∞ for our $64 \times 64 \times 64$ grid.

N_A	$(\chi N)_{\text{ODT}}$	L_α/R_0	z_∞
38	13.75	7.40	0.783
37	13.65	7.35	0.781
36	13.75	7.31	0.779
35	13.95	7.24	0.777
34	14.15	7.28	0.778

D. Cylinder-disorder transition

For the cylindrical phase, we start with an orthorhombic box of appropriate dimensions so as to spontaneously form one unit cell of cylinders oriented in the x direction. Once the cylinders form, we periodically repeat the morphology creating a box with 6 unit cells (see the inset of Fig. 9). The box move is then applied with the aspect ratio in the y - z plane fixed at $L_y/L_z = 2/\sqrt{3}$. In this case, the equilibrium periodicity agrees with the SCFT prediction to within 1%. Once the preferred period is determined, the box dimensions are fixed, and $S(k)$ is calculated for a series of χN values.

Figure 9 shows $S(k)$ at several different values of χN for $N_A = 30$. Interestingly, the usual Bragg reflections for the hexagonal symmetry are accompanied by weak secondary peaks at a slightly higher wavevector, k . These are due to lateral fluctuations of the cylinders with a wavelength equal to L_x . In an infinite box, these fluctuations would occur over a distribution of wavelengths and, thus, would not create separate peaks. Nevertheless, the ODT is clearly identified at $(\chi N)_{\text{ODT}} = 14.85 \pm 0.05$. Results for other compositions are listed in

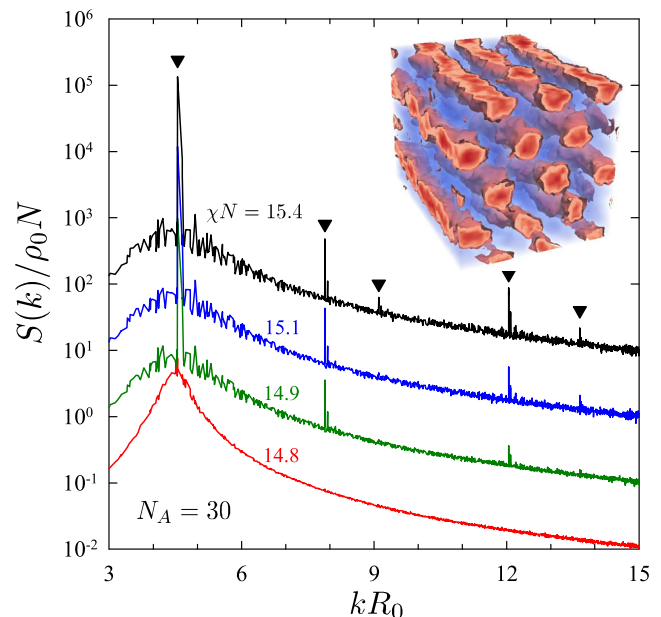


FIG. 9. Analogous plot to that of Fig. 6, but for diblocks with $N_A = 30$ and $N_B = 60$. The morphology (see the inset) and peak positions (triangles) confirm that the ordered state is cylinders.

TABLE IV. Cylinder-disorder transitions, sizes of the simulation box ($L_x = 6.4R_0$ and $L_z = \sqrt{3}/4L_y$), and the z_∞ for our $64 \times 48 \times 48$ grid.

N_A	$(\chi N)_{\text{ODT}}$	L_y/R_0	z_∞
34	14.15	5.56	0.737
32	14.25	5.53	0.736
30	14.85	5.52	0.736
28	15.55	5.48	0.735
26	16.55	5.47	0.735

Table IV. When attempting to locate a cylinder-disorder transition at $N_A = 35$, connections would form between the cylinders creating a network structure prior to disordering. Evidently, gyroid is preferred over cylinders at this composition, which is to be expected based on the SCFT phase diagram.

E. Sphere-disorder transition

When attempting to locate a cylinder-disorder transition at $N_A = 24$, the cylinders pinch off into a series of spheres as χN is decreased. However, in this case, the spheres are unable to adopt a bcc lattice due to the orthorhombic simulation box. Therefore, we switch to a cubic box of appropriate size (based on SCFT) to form a single unit cell of bcc spheres. Once the spheres spontaneously form from disorder, the morphology is periodically repeated, creating a cubic simulation box of 27 unit cells. As before, the preferred size of the box is deduced by maximizing the strength of the scattering peaks. In this case, the preferred size is about 1% smaller than the SCFT prediction.

Figure 10 shows $S(k)$ evaluated at a series of χN values, which imply an ODT of $(\chi N)_{\text{ODT}} = 18.05 \pm 0.05$, as listed in **Table V**. The simulation at $\chi N = 18.1$ produces peaks consistent with the bcc spherical phase, as confirmed by inspection of the morphology (see the inset). However, increasing the segregation to $\chi N = 18.2$ causes the spheres to fuse together forming cylinders oriented in the (111) direction. This is also accompanied by the extinction of Bragg reflections, leaving just the peaks consistent with the hexagonal symmetry. Interestingly, the morphology switches back to spheres when the segregation is returned to $\chi N = 18.1$. Hence, this composition exhibits a relatively facile epitaxial $C \leftrightarrow S$ transition⁴⁷ at $(\chi N)_{\text{ODT}} = 18.15 \pm 0.05$.

F. Phase diagram

Figure 11 compares our ODT predictions to the mean-field phase boundaries from **Fig. 1(a)**. As expected, the ODT is shifted upward relative to the mean-field prediction. Interestingly, the shift is reasonably uniform across the whole range of compositions considered in our study, which is consistent with particle-based

TABLE V. Sphere-disorder transition, size of the simulation box, and the z_∞ for our $48 \times 48 \times 48$ grid.

N_A	$(\chi N)_{\text{ODT}}$	L_α/R_0	z_∞
24	18.05	5.71	0.790

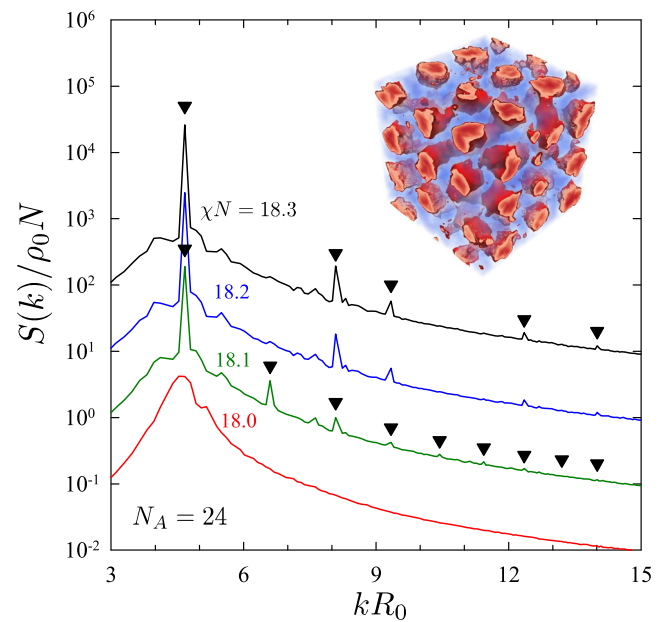


FIG. 10. Analogous plot to that of **Fig. 6**, but for diblocks with $N_A = 24$ and $N_B = 66$. The morphology (see the inset) and peak positions (lower triangles) at $\chi N = 18.1$ confirm that the ordered state is bcc spheres. However, the morphology (not shown) and peak positions (upper triangles) at $\chi N = 18.2$ and 18.3 correspond to hexagonally packed cylinders.

simulations that observe shifts of 2.61^{48} and 2.65^{35} at $f = 0.25$ and 0.5 , respectively. However, the shift predicted by FTS is somewhat smaller by about 0.4 , which we attribute to inaccuracy in the linear $\chi \approx z_\infty \chi_b$.

As expected, the ordered phases along the ODT agree well with the relative stabilities predicted by SCFT. For most compositions,

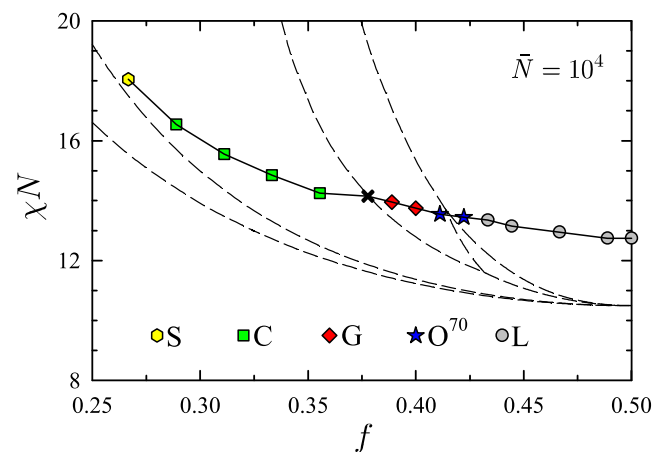


FIG. 11. Order-disorder transitions for conformationally symmetric diblock copolymers of invariant polymerization index $\bar{N} = 10^4$. The different symmetries of the ordered phases are denoted by circles (L), stars (O^{70}), diamonds (G), squares (C), and hexagons (S). The cross marks the ODT for which the relative stability of C and G was indistinguishable. Dashed curves show the mean-field phase boundaries from **Fig. 1(a)**.

the preferred morphology is obvious from the simulations, but at several compositions, there are closely competing morphologies. In most instances, the stable ordered phase can be ascertained based on which survives to lowest χN . The only exception is at $N_A = 34$ (denoted by a cross in Fig. 11), where the cylindrical and gyroid phases both remain stable down to $\chi N = 14.2$. Nevertheless, this is perfectly consistent with the fact that the ODT coincides closely with the C–G boundary in the SCFT phase diagram.

IV. DISCUSSION

Our predictions for the complex phase behavior agree nicely with experiments. It is well-established that fluctuations cause direct gyroid–disorder transitions, and this even appears to be the case for large PE-PEP diblocks of $\tilde{N} \approx 2.5 \times 10^4$. Although the experiments actually observe direct transitions with perforated lamellae instead of gyroid,¹³ this is understood to be a result of slow dynamics. Experiments^{49,50} and theory⁵¹ find that the perforated-lamellar phase is generally a metastable state that transforms to gyroid given sufficient time. More significantly, our study provides the first theoretical corroboration for the observation of the Fddd phase in PS-PI diblocks of $\tilde{N} \approx 1.1 \times 10^3$.^{10,23}

Not surprisingly, our FTS provide further conformation that the Landau–Brazovskii theory used to generate the fluctuation-corrected phase diagram in Fig. 1(b)¹⁵ is seriously inaccurate. Just as it fails to predict stable spheres, it also fails to predict the Fddd phase. It does predict a gyroid–disorder transition, but with an unrealistically narrow width of $\Delta f \approx 0.004$. Furthermore, the Landau–Brazovskii theory significantly underestimates the fluctuation-induced shift of the ODT, as compared to our FTS as well as previous particle-based simulations.^{35,48,52–54}

It is also interesting to compare our results from Langevin FTS to those obtained from complex Langevin FTS.^{18,22} Although we cannot compare the relative shifts in the ODT because the CL-FTS have yet to be expressed in terms of an effective χ , we can, nevertheless, compare the sequence of ordered phases along the ODT. The results of Lennon *et al.*¹⁸ are reasonably consistent with ours, if one takes into account that their \tilde{N} is much larger and that they did not consider the Fddd phase. Unfortunately, the accuracy of those results has now been called into question.²² Still, there are the more recent CL-FTS for $\tilde{N} \approx 10^4$ by Delaney and Fredrickson.²² However, the complex phase behavior is very different; they observe no Fddd phase nor even a direct gyroid–disorder transition.

One potential source of discrepancy with CL-FTS is the partial saddle-point approximation used by L-FTS. Given that fluctuations in $W_+(\mathbf{r})$ are expected to be far less important than those in $W_-(\mathbf{r})$, it is unlikely that this could be responsible for such serious qualitative differences. Indeed, past studies^{26,28} have found the partial saddle-point approximation to be accurate. The only evidence of inaccuracy^{27,30} has been the inability of L-FTS to capture the departure of $S(k^*)$ from the RPA prediction at small χN as predicted by ROL.^{37,55} However, this inaccuracy is fairly mild even for $\tilde{N} \approx 10^3$ and virtually nonexistent for $\tilde{N} \gtrsim 10^4$.

The more significant sources of discrepancy are likely the differences between the models. We use discrete rather than continuous Gaussian chains, while Delaney and Fredrickson²² introduce compressibility and smear the interactions. It is important that none of these modifications to the standard GCM are so severe so as to

destroy universality. One can gauge their impact by examining the effect on the SCFT phase diagram. In this regard, the SCFT calculations in Ref. 38 demonstrate that the effect of using discrete chains is relatively minor for $N = 90$, which is also the case in particle-based simulations.^{35,48,52–54} Likewise, the compressibility used in the CL-FTS also appears to have a minimal effect. On the other hand, the smearing causes a considerable perturbation to the SCFT phase diagram. Its purpose is to remove the UV divergence, allowing for convergent results once the grid size becomes sufficiently small relative to the range of the interactions. However, for universality to hold, the range also needs to be small relative to all relevant coarse-grained length scales, including the width of the internal A/B interfaces. It seems that this may not have been the case. Unfortunately, a reduction in the range requires a similar reduction in the grid spacing, which is probably not computationally feasible.

The fact that the periodicities of our ordered phases coincide well with SCFT is consistent with previous FTS^{27,29} as well as numerous particle-based simulations.^{48,52–54} Delaney and Fredrickson also found similar agreement for the lamellar phase, which led them to use SCFT predictions for the non-lamellar phases. However, this is not equivalent. The former examples involve comparisons to SCFT predictions of the standard GCM evaluated at the effective χ , whereas the agreement observed by Delaney and Fredrickson is for the SCFT of their modified model evaluated at the bare χ_b . The former agreement is expected to be general, while the latter agreement may have occurred just because the comparison was performed at an exceptionally large $\tilde{N} = 5.4 \times 10^5$, where fluctuations are greatly reduced as are the potential differences between SCFT and FTS.

Our current study has improved the FTS by doing away with the continuous Gaussian chain, for which integrating over the contour represents a serious numerical challenge. In SCFT, accurate results are readily obtained using the pseudo-spectral algorithm combined with Richardson extrapolation,^{42,56} but in FTS, the fluctuations degrade the effectiveness of higher-order schemes such as Richardson extrapolation.²¹ In a previous study,³⁰ we dealt with this by considering the numerical method and its finite integration step as part of the model, and then, we mapped the system back onto the standard GCM using the Morse calibration. Here, the issue is avoided altogether by switching to a chain of N discrete beads. As previously mentioned, N must be sufficient to ensure that universality holds. Particle-based simulations suggest that $N \gtrsim 30$ would suffice,^{35,48,52} but to be certain, we chose $N = 90$. This has the added benefit of providing finer resolution in composition, although increased resolution could also be achieved by blending diblocks of neighboring compositions,⁵⁷ a strategy used in experiments.⁹

As before,³⁰ the modification of the model is compensated for by the Morse calibration. This time, however, we just use the linear $\chi \approx z_\infty \chi_b$, which is expected to be reasonably accurate at $\tilde{N} = 10^4$.^{30,35,53} While the linear approximation can be calculated analytically, the nonlinear calibration requires simulations of $S(k)$ over the disordered phase.³⁰ The computational cost would be considerable given that the calibration needs to be repeated for each different grid resolution. In any case, this would simply shift the ODT upward by some small amount and would not change the ordered phases along the ODT. We have, nevertheless, ensured that sufficient information regarding the grid resolutions is provided so that the nonlinear calibration could be performed at a later time.

V. SUMMARY

Using field-theoretic simulations (FTS),^{6,17} we evaluated the order–disorder transition (ODT) for diblock copolymer melts of invariant polymerization index $\bar{N} = 10^4$. The ODT was located by examining the disappearance of peaks in the structure function, $S(k)$, in much the same way as it is detected in experiments. The symmetries of the ordered phases were identified by visual inspection of the composition field and confirmed by the peak positions of $S(k)$. Our results provide the first theoretical evidence that the complex Fddd phase in Fig. 1(a) survives fluctuation effects, consistent with its experimental observation in PS-PI diblock melts.^{10,23} They also show that, even at the relatively large $\bar{N} = 10^4$, fluctuations are sufficient to cause direct gyroid–disorder transitions, consistent with experiments of PE-PEP diblock melts.¹³ Note that the latter conclusion assumes that the perforated-lamellar phase observed in diblock melts is an intermediate state that eventually converts to the gyroid phase.^{49–51}

Our implementation of FTS used a partial saddle-point approximation for the pressure field that enforces incompressibility,^{6,26} which removes an instability that hinders the fully fluctuating version of FTS.^{20–22} The approximation is expected to be accurate for the large \bar{N} considered in this study.^{6,26,28} We also switched the FTS model from continuous to discrete Gaussian chains, which removes the source of numerical inaccuracy associated with the usual integration along the chain contours. The polymer chains, nevertheless, contained an ample number of monomers, $N = 90$, to ensure that the simulations adhere to universality.

The change to discrete chains as well as the UV divergence were accounted for by a linear renormalization of the interaction parameter, $\chi \approx z_\infty \chi_b$, where z_∞ is the fraction of intermolecular contacts in the limits of $\chi_b \rightarrow 0$ and $N \rightarrow \infty$.¹ Comparison of our ODT with universal predictions at $f = 0.5$ ³⁵ and $f = 0.25$ ⁴⁸ indicates that the linear approximation causes a small underestimation of $(\chi N)_{\text{ODT}}$ by about 0.4. The Morse calibration³⁴ could provide a more accurate nonlinear χ by matching the peak of the disordered-state structure function, $S(k)$, to ROL predictions, as illustrated in Ref. 30. Nevertheless, this would not alter the sequence of ordered phases along the ODT, and therefore, we leave it for future consideration.

ACKNOWLEDGMENTS

Computer resources were provided by Compute Canada.

DATA AVAILABILITY

The data that support the findings of this study are available from the corresponding author upon reasonable request.

REFERENCES

- J. Glaser, J. Qin, P. Medapuram, M. Müller, and D. C. Morse, “Test of a scaling hypothesis for the structure factor of disordered diblock copolymer melts,” *Soft Matter* **8**, 11310–11317 (2012).
- M. W. Matsen, “The standard Gaussian model for block copolymer melts,” *J. Phys.: Condens. Matter* **14**, R21–R47 (2002).
- M. W. Matsen and F. S. Bates, “Unifying weak- and strong-segregation block copolymer theories,” *Macromolecules* **29**, 1091–1098 (1996).
- G. H. Fredrickson, *The Equilibrium Theory of Inhomogeneous Polymers* (Oxford University Press, New York, 2006).
- M. W. Matsen, in *Soft Matter: Polymer Melts and Mixtures*, edited by G. Gompper and M. Schick (Wiley VCH, Weinheim, Germany, 2006).
- M. W. Matsen, “Field theoretic approach for block polymer melts: SCFT and FTS,” *J. Chem. Phys.* **152**, 110901 (2020).
- The constant originates from the first term in the identity $\phi_A \phi_B = (1 - \phi_-^2)/4$, where $\phi_- \equiv \phi_A - \phi_B$.
- D. A. Hajduk, P. E. Harper, S. M. Gruner, C. C. Honeker, G. Kim, and E. L. Thomas, “The gyroid: A new equilibrium morphology in weakly segregated diblock copolymers,” *Macromolecules* **27**, 4063–4075 (1994).
- M. F. Schulz, F. S. Bates, K. Almdal, and K. Mortensen, “Epitaxial relationship for hexagonal-to-cubic phase transition in a block copolymer mixture,” *Phys. Rev. Lett.* **73**, 86–89 (1994).
- M. Takenaka, T. Wakada, S. Akasaka, S. Nishitsuji, K. Saijo, H. Shimizu, M. I. Kim, and H. Hasegawa, “Orthorhombic Fddd network in diblock copolymer melts,” *Macromolecules* **40**, 4399–4402 (2007).
- G. H. Fredrickson and E. Helfand, “Fluctuation effects in the theory of microphase separation in block copolymers,” *J. Chem. Phys.* **87**, 697–705 (1987).
- S. A. Brazovskii, “Phase transition of an isotropic system to a nonuniform state,” *Sov. Phys. JETP* **41**, 85–89 (1975).
- F. S. Bates, M. F. Schulz, A. K. Khandpur, S. Förster, and J. H. Rosedale, “Fluctuations, conformational asymmetry and block copolymer phase behaviour,” *Faraday Discuss.* **98**, 7–18 (1994).
- I. W. Hamley and V. E. Podnec, “On the Landau-Brazovskii theory for block copolymer melts,” *Macromolecules* **30**, 3701–3703 (1997).
- B. Miao and R. A. Wickham, “Fluctuation effects and the stability of the Fddd network phase in diblock copolymer melts,” *J. Chem. Phys.* **128**, 054902 (2008).
- V. Ganesan and G. H. Fredrickson, “Field-theoretic polymer simulations,” *Europhys. Lett.* **55**, 814–820 (2001).
- G. H. Fredrickson, V. Ganesan, and F. Drolet, “Field-theoretic computer simulation methods for polymers and complex fluids,” *Macromolecules* **35**, 16–39 (2002).
- E. M. Lennon, K. Katsov, and G. H. Fredrickson, “Free energy evaluation in field-theoretic polymer simulations,” *Phys. Rev. Lett.* **101**, 138302 (2008).
- C. T. Tyler and D. C. Morse, “Orthorhombic Fddd network in triblock and diblock copolymer melts,” *Phys. Rev. Lett.* **94**, 208302 (2005).
- J. Koski, H. Chao, and R. A. J. Riggelman, “Field theoretic simulations of polymer nanocomposites,” *J. Chem. Phys.* **139**, 244911 (2013).
- D. J. Audus, K. T. Delaney, H. D. Ceniceros, and G. H. Fredrickson, “Comparison of pseudospectral algorithms for field-theoretic simulations of polymers,” *Macromolecules* **46**, 8383–8391 (2013).
- K. T. Delaney and G. H. Fredrickson, “Recent developments in fully fluctuating field-theoretic simulations of polymer melts and solutions,” *J. Phys. Chem. B* **120**, 7615–7634 (2016).
- Y.-C. Wang, K. Matsuda, M. I. Kim, A. Miyoshi, S. Akasaka, S. Nishitsuji, K. Saijo, H. Hasegawa, K. Ito, T. Hikima, and M. Takenaka, “Fddd phase boundary of polystyrene-block-polyisoprene diblock copolymer melts in the polystyrene-rich region,” *Macromolecules* **48**, 2211–2216 (2015).
- M. W. Matsen, “Fast and accurate SCFT calculations for periodic block-copolymer morphologies using the spectral method with Anderson mixing,” *Eur. Phys. J. E* **30**, 361–369 (2009).
- E. Reister, M. Müller, and K. Binder, “Spinodal decomposition in a binary polymer mixture: Dynamic self-consistent-field theory and Monte Carlo simulations,” *Phys. Rev. E* **64**, 041804 (2001).
- D. Dücks, V. Ganesan, G. H. Fredrickson, and F. Schmid, “Fluctuation effects in ternary AB+A+B polymeric emulsions,” *Macromolecules* **36**, 9237–9248 (2003).
- T. M. Beardsley, R. K. W. Spencer, and M. W. Matsen, “Computationally efficient field-theoretic simulations for block copolymer melts,” *Macromolecules* **52**, 8840–8848 (2019).
- A. Alexander-Katz and G. H. Fredrickson, “Diblock copolymer thin films: A field-theoretic simulation study,” *Macromolecules* **40**, 4075–4087 (2007).

- ²⁹B. Vorselaars, P. Stasiak, and M. W. Matsen, “Field-theoretic simulation of block copolymers at experimentally relevant molecular weights,” *Macromolecules* **48**, 9071–9080 (2015).
- ³⁰T. M. Beardsley and M. W. Matsen, “Calibration of the Flory-Huggins interaction parameter in field-theoretic simulations,” *J. Chem. Phys.* **150**, 174902 (2019).
- ³¹M. Olvera de la Cruz, S. F. Edwards, and I. C. Sanchez, “Concentration fluctuations in polymer blend thermodynamics,” *J. Chem. Phys.* **89**, 1704–1708 (1988).
- ³²P. Stasiak and M. W. Matsen, “Monte Carlo field-theoretic simulations for melts of symmetric diblock copolymer,” *Macromolecules* **46**, 8037–8045 (2013).
- ³³P. Grzywacz, J. Qin, and D. C. Morse, “Renormalization of the one-loop theory of fluctuations in polymer blends and diblock copolymer melts,” *Phys. Rev. E* **76**, 061802 (2007).
- ³⁴J. Qin and D. C. Morse, “Renormalized one-loop theory of correlations in polymer blends,” *J. Chem. Phys.* **130**, 224902 (2009).
- ³⁵J. Glaser, P. Medapuram, T. M. Beardsley, M. W. Matsen, and D. C. Morse, “Universality of block copolymer melts,” *Phys. Rev. Lett.* **113**, 068302 (2014).
- ³⁶J. Glaser, P. Medapuram, and D. C. Morse, “Collective and single-chain correlations in disordered melts of symmetric diblock copolymers: Quantitative comparison of simulations and theory,” *Macromolecules* **47**, 851–869 (2014).
- ³⁷J. Qin, P. Grzywacz, and D. C. Morse, “Renormalized one-loop theory of correlations in disordered diblock copolymers,” *J. Chem. Phys.* **135**, 084902 (2011).
- ³⁸M. W. Matsen, “Self-consistent field theory for melts of low-molecular-weight diblock copolymer,” *Macromolecules* **45**, 8502–8509 (2012).
- ³⁹D. G. Anderson, “Iterative procedures for nonlinear integral equations,” *J. Assoc. Comput. Mach.* **12**, 547–560 (1965).
- ⁴⁰R. B. Thompson, K. Ø. Rasmussen, and T. Lookman, “Improved convergence in block copolymer self-consistent field theory by Anderson mixing,” *J. Chem. Phys.* **120**, 31–34 (2004).
- ⁴¹For our particular case, we set the $d_j^{(k)}$ in Eq. (12) of Ref. 42 to the value of $\phi_+(r) - 1$ evaluated at the j th mesh point.
- ⁴²P. Stasiak and M. W. Matsen, “Efficiency of pseudo-spectral algorithms with Anderson mixing for the SCFT of periodic block-copolymer phases,” *Eur. Phys. J. E* **34**, 110 (2011).
- ⁴³D. Düchs, K. T. Delaney, and G. H. Fredrickson, “A multi-species exchange model for fully fluctuating polymer field theory simulations,” *J. Chem. Phys.* **141**, 174103 (2014).
- ⁴⁴R. A. Riggleman and G. H. Fredrickson, “Field-theoretic simulations in the Gibbs ensemble,” *J. Chem. Phys.* **132**, 024104 (2010).
- ⁴⁵R. K. W. Spencer, B. Vorselaars, and M. W. Matsen, “Continuous thermodynamic integration in field-theoretic simulations of structured polymers,” *Macromol. Theory Simul.* **26**, 1700036 (2017).
- ⁴⁶*International Tables for X-Ray Crystallography*, edited by N. F. M. Henry and K. Lonsdale (Kynoch, Birmingham, 1969).
- ⁴⁷M. W. Matsen, “Cylinder \leftrightarrow sphere epitaxial transitions in block copolymer melts,” *J. Chem. Phys.* **114**, 8165–8173 (2001).
- ⁴⁸T. Ghasimakbari and D. C. Morse, “Order-disorder transitions and free energies in asymmetric diblock copolymers,” *Macromolecules* **53**, 7399–7409 (2020).
- ⁴⁹D. A. Hajduk, H. Takenouchi, M. A. Hillmyer, F. S. Bates, M. E. Vigild, and K. Almdal, “Stability of the perforated layer (PL) phase in diblock copolymer melts,” *Macromolecules* **30**, 3788–3795 (1997).
- ⁵⁰M. E. Vigild, K. Almdal, K. Mortensen, I. W. Hamley, J. P. A. Fairclough, and A. J. Ryan, “Transformations to and from the gyroid phase in a diblock copolymer,” *Macromolecules* **31**, 5702–5716 (1998).
- ⁵¹X. Cheng, L. Lin, Weinan E, P. Zhang, and A.-C. Shi, “Nucleation of ordered phases in block copolymers,” *Phys. Rev. Lett.* **104**, 148301 (2010).
- ⁵²P. Medapuram, J. Glaser, and D. C. Morse, “Universal phenomenology of symmetric diblock copolymers near the order-disorder transition,” *Macromolecules* **48**, 819–839 (2015).
- ⁵³J. D. Willis, T. M. Beardsley, and M. W. Matsen, “Calibration of a lattice model for high-molecular-weight block copolymer melts,” *J. Chem. Phys.* **150**, 204906 (2019).
- ⁵⁴J. D. Willis, T. M. Beardsley, and M. W. Matsen, “A simple and accurate method to determine the Flory-Huggins χ parameter,” *Macromolecules* **53**, 9973–9982 (2020).
- ⁵⁵J. Qin and D. C. Morse, “Fluctuations in symmetric diblock copolymers: Testing theories old and new,” *Phys. Rev. Lett.* **108**, 238301 (2012).
- ⁵⁶A. Ranjan, J. Qin, and D. C. Morse, “Linear response and stability of ordered phases of block copolymer melts,” *Macromolecules* **41**, 942–954 (2008).
- ⁵⁷M. W. Matsen and F. S. Bates, “One-component approximation for binary diblock copolymer blends,” *Macromolecules* **28**, 7298–7300 (1995).